A Theory of microresonator based frequency comb generation

A.1 Optical coupling to microresonators

A light field $\tilde{A} = A(t)\,e^{-i\omega_0 t}$ at resonance frequency ω_0 inside a weakly damped resonator can be described in by its rotating frame amplitude A, which we normalize such that $|A|^2$ corresponds to the number of photons in the resonator mode. The time evolution of this light field is given by

$$\frac{\mathrm{d}A(t)}{\mathrm{d}t} = -\frac{\kappa_0}{2} A(t) \tag{A.1}$$

where κ_0 denotes the intrinsic cavity decay rate. To maintain a steady intracavity field a driving field (pump laser) is coupled to the resonator:

$$\frac{\mathrm{d}A(t)}{\mathrm{d}t} = -\frac{\kappa}{2} A(t) + \sqrt{\kappa_{\mathrm{ext}}}\, s_{\mathrm{in}}(t)\, e^{-i(\omega_{\mathrm{p}}-\omega_0)t} \tag{A.2}$$

The last phase factor accounts for the fact that the pump frequency ω_{p} may be detuned from the resonance frequency ω_0. As the coupling between driving field s_{in} and the resonator introduces another loss mechanism the intrinsic cavity decay rate κ_0 is replaced by the combined decay rate $\kappa = \kappa_0 + \kappa_{\mathrm{ext}}$, where κ_{ext} denoted the coupling rate. The ratio of $\eta = \kappa_{\mathrm{ext}}/\kappa$ is called coupling ratio and allows to distinguish three coupling regimes that is undercoupled ($\kappa_{\mathrm{ext}} < \kappa_0$), overcoupled ($\kappa_{\mathrm{ext}} > \kappa_0$) and critically coupled ($\kappa_{\mathrm{ext}} = \kappa_0$).

Applying the phase transformation $a = A\,e^{i(\omega_{\mathrm{p}}-\omega_0)t}$ translates eq. (A.2) from the rotating frame of the resonant field ω_0 into the rotating frame of the driven cavity field defined by the pump frequency ω_{p}:

$$\frac{\mathrm{d}a(t)}{\mathrm{d}t} = -\left(i(\omega_0 - \omega_{\mathrm{p}}) + \frac{\kappa}{2}\right) a(t) + \sqrt{\kappa_{\mathrm{ext}}}\, s_{\mathrm{in}}(t) \tag{A.3}$$

This allows for the derivation of the steady state intracavity field amplitude a assuming constant driving conditions $s_{in}(t) = s_{in}$

$$a = \frac{\sqrt{\kappa_{ext}}}{i(\omega_0 - \omega_p) + (\frac{\kappa}{2})} \cdot s_{in} \tag{A.4}$$

and the steady state photon number inside the cavity:

$$|a|^2 = \frac{\kappa_{ext}}{(\omega_0 - \omega_p)^2 + (\frac{\kappa}{2})^2} \cdot |s_{in}|^2 \tag{A.5}$$

Coupled resonator transmission

Energy conservation dictates that the photon flux $|s_{out}|^2$ equals the difference between incoming photon flux $|s_{in}|^2$ and dissipated photons inside the cavity:

$$|s_{out}|^2 = |s_{in}|^2 - \kappa_0 |a|^2 = \left(1 - \frac{\kappa_{ext}\kappa_0}{(\omega_0 - \omega_p)^2 + (\frac{\kappa}{2})^2}\right) \cdot |s_{in}|^2 \tag{A.6}$$

The transmitted power $\hbar\omega_p |s_{out}|^2$ is usually detected on a photo-detector and used for monitoring purposes. The transmission is described by a Lorentzian resonance dip with full width at half maximum (FWHM) of κ and relative depth $1 - |s_{out}|^2/|s_{in}|^2 = \kappa_{ext}\kappa_0/\kappa^2$. Full extinction of the transmission can be achieved under critical coupling conditions $\kappa_{ext} = \kappa_0 = \kappa/2$. In this case the full power launched into the waveguide is dissipated in the resonator.

Circulating power P_{cav} and finesse

The circulating power P_{cav} inside the cavity can be found by multiplying eq. (A.5) with the photon energy $\hbar\omega_p$ and division by the roundtrip time $T_R = 1/FSR$:

$$P_{cav} = FSR \cdot \frac{\kappa_{ext}}{(\omega_0 - \omega_p)^2 + (\frac{\kappa}{2})^2} \cdot P_{in} = 2\eta \cdot \frac{F}{\pi} \cdot \frac{1}{\left(\frac{4(\omega_0 - \omega_p)^2}{\kappa^2}\right) + 1} \cdot P_{in} \tag{A.7}$$

In the above equation we have introduced the finesse of the resonator as the ratio between FSR and linewidth:

$$F = \frac{FSR}{\kappa/2\pi} \tag{A.8}$$

The circulating power inside the resonator is proportional to the finesse F and reaches is maximal value in the case of zero detuning $\omega_{\mathrm{p}} = \omega_0$ and critical coupling $\eta = 1/2$:

$$P_{\mathrm{cav}} = \frac{F}{\pi} \cdot P_{\mathrm{in}} \tag{A.9}$$

A.2 Frequency comb formation in microresonators

In the following the above formalism will be extended to the case of many nonlinearly coupled optical modes in a resonator with dispersion. These (nonlinear) coupled mode equations[71, 141, 142, 144, 189, 190] allow for analytic derivation of e.g. the threshold pump power and also serve as a basis for numeric simulations used in Chapter 4.

A.2.1 Nonlinear coupled mode equations

The FWM dynamics in a microresonator can be described using a system of nonlinear coupled mode equations. To this end eq. A.2 needs to be written for all modes with mode number μ and extended by a nonlinear coupling term that accounts for the interaction between the modes enabled by the $\chi^{(3)}$-nonlinearity. The pump term will only be kept for the mode with relative mode number $\mu = 0$.

Derivation of the nonlinear coupling term

We start out with the scalar wave a equation[135]

$$\frac{1}{R^2}\frac{\partial^2}{\partial\phi^2}E(t,\phi) - \frac{n_0^2}{c^2}\frac{\partial^2}{\partial t^2}E(t,\phi) = \frac{1}{\epsilon_0 c^2}\frac{\partial^2}{\partial t^2}P_{\mathrm{NL}}(t,\phi), \tag{A.10}$$

where the spatial coordinate z has been replaced by the angular coordinate ϕ to account for the closed geometry of the resonator (without loss of generality a circular resonator with radius R is assumed). To mathematically describe the nonlinear polarization

$$P_{\mathrm{NL}}(t,\phi) = \epsilon_0 \chi^{(3)} E(t,\phi)^3, \tag{A.11}$$

we expand the electric field in field components at the resonance frequencies ω_ν of the resonator. This approximation is justified by the low losses of high-Q microresonators and the resulting narrow resonances. In the expansion we use the normalised field

amplitudes A_ν normalized such that $|A_\nu|^2$ is the number of photons in the mode ν:

$$E(t,\phi) = \frac{1}{2} \sum_\nu \sqrt{\frac{2\hbar\omega_\nu}{n_0^2\epsilon_0 V_{\text{eff}}}} A_\nu(t) e^{i(\nu\phi-\omega_\nu t)} + c.c. \tag{A.12}$$

$A_\nu(t)$ describes the slowly varying envelope of the field that is changing only on times scales that are much longer then the period ω_ν^{-1} of the carrier frequency. In particular, $A_\nu(t)$ is assumed to remain approximately constant over one resonator roundtrip. We note that the comb lines do not need to oscillate at the exact same frequency as the resonator modes. A deviation of the comb mode frequency from the resonance frequency ω_ν will be contained in $A_\nu(t)$.

Inserting eq. A.12 into eq. A.10 and projecting onto a particular mode A_μ i.e. multiplication with $A_\mu(t)^* e^{-i(\mu\phi-\omega_\mu t)}$ and integration over the spatial coordinate ϕ eventually results in:

$$\frac{\partial A_\mu}{\partial t} = ig \sum_{\mu',\mu'',\mu'''} A_{\mu'} A_{\mu''} A_{\mu'''}^* e^{-i(\omega_{\mu'}+\omega_{\mu''}-\omega_{\mu'''}-\omega_\mu)} \tag{A.13}$$

In the last step terms with negative frequencies as well as terms of the form $A_{\mu'} A_{\mu''} A_{\mu'''}$ that describe tripe sum frequency and third harmonic generation have been omitted. The nonlinear coupling coefficient

$$g = \frac{\hbar\omega_0^2 c n_2}{n_0^2 V_{\text{eff}}}. \tag{A.14}$$

describes the $\chi^{(3)}$-nonlinearity of the system with the refractive index n_0, nonlinear refractive index n_2, the effective nonlinear cavity volume $V_{\text{eff}} = A_{\text{eff}} L$ (resonator length L), the speed of light c and $\hbar$ the Planck constant devided by 2π. Physically g can be interpreted as the per photon frequency shift of the resonance frequency due to the Kerr-nonlinearity (via SPM). The summation is done for all μ', μ'', μ''' respecting the relation $\mu = \mu' + \mu'' - \mu'''$.

The full coupled mode equation

The full nonlinear coupled mode equations including the pump term as well as the cavity loss are:

$$\frac{\partial A_\mu}{\partial t} = -\frac{\kappa}{2} A_\mu + \delta_{\mu 0} \sqrt{\kappa_{\text{ext}}} s_{\text{in}} e^{-i(\omega_p-\omega_0)t}$$
$$+ ig \sum_{\mu',\mu'',\mu'''} A_{\mu'} A_{\mu''} A_{\mu'''}^* e^{-i(\omega_{\mu'}+\omega_{\mu''}-\omega_{\mu'''}-\omega_\mu)t} \tag{A.15}$$

Without loss of generality the initial phase of the pump is set to zero while $s = \sqrt{P_{\text{in}}/\hbar\omega_0}$ denotes the amplitude of the pump power P_{in} coupled to the cavity and $\delta_{\mu 0}$ is the Kronecker delta. The transmitted power through the coupling waveguide s_{out} is described by

$$s_{\text{out}} = s_{\text{in}} - \sqrt{\eta\kappa} \sum A_\mu\, e^{-i(\omega_\mu - \omega_p)t}. \tag{A.16}$$

In the above equations it is assumed that neither the resonator to waveguide coupling, nor the nonlinearty or resonator loss depends on the optical wavelength. Moreover, we assume unity mode overlap for all wavelength. Also, particularities of the resonator geometry and interaction with other mode families are not taken into account.

Using the expression for the cold cavity resonance frequencies $\omega_\mu = \omega_0 + D_1\mu + \frac{1}{2}D_2\mu^2$ (cf. eq. 1.4 in Section 1.2.1) the system of equations may be written in a dimensionless way[141]: $f = \sqrt{8\eta g/\kappa^2}\,s$, $d_2 = D_2/\kappa$, $\zeta_\mu = 2(\omega_\mu - \omega_p - \mu D_1)/\kappa = \zeta_0 + d_2\mu^2$, $\tau = \kappa t/2$. Moreover, the phase transformation $a_\mu = A_\mu \sqrt{2g/\kappa}\,e^{-i(\omega_\mu - \omega_p - \mu D_1)t}$ is applied to achieve time-independence of the nonlinear terms:

$$\begin{aligned}
\frac{\partial a_\mu}{\partial \tau} &= -[1 + i\zeta_\mu]a_\mu \\
&\quad + i \sum_{\mu' \leq \mu''} (2 - \delta_{\mu'\mu''})a_{\mu'}a_{\mu''}a_{\mu'+\mu''-\mu}^* + \delta_{0\mu}f
\end{aligned} \tag{A.17}$$

In this form all frequencies, detunings and magnitudes are measured in units of half resonance linewidth $\kappa/2$. As opposed to the modes A_μ, the fields a_μ correspond to an equidistant frequency grid. Note that amplitude and phase modulation implicitly included in the time dependence of a_μ include frequency deviations form the equidistant grid and in particular noisy comb states with multiple lines per resonance. For the stationary soliton solutions discussed in the main text and later on here, the amplitudes and phases of a_μ are constant in time when third and higher order dispersion is neglected.

A.2.2 Three mode system

To determine the parametric threshold and the first oscillating mode it is sufficient to consider a three mode system of a_0, $a_{+\mu}$, and $a_{-\mu}^*$,[142] i.e. pump as well as two first primary sidebands emerging in the resonator modes indexed $+\mu$ and $-\mu$.

The equation for the pump reads

$$\frac{\partial a_0}{\partial \tau} = -[1 + i\zeta_0 - i|a_0|^2]a_0 + f \tag{A.18}$$

and requiring $\partial a_0/\partial\tau = 0$ we find for the steady state (as long as no sidebands are

excited):

$$(\zeta_0 - |a_0|^2)^2 |a_0|^2 + |a_0|^2 = f^2. \tag{A.19}$$

The linearised equations describing the sidebands read:

$$\frac{\partial a_{+\mu}}{\partial \tau} = -[1 + i\zeta_\mu - 2i|a_0|^2]a_{+\mu} + ia_0^2 a_{-\mu}^*,$$

$$\frac{\partial a_{-\mu}^*}{\partial \tau} = -[1 - i\zeta_\mu + 2i|a_0|^2]a_{-\mu}^* - ia_0^{*2} a_{+\mu}. \tag{A.20}$$

This system of linear equations can be written in matrix form

$$\begin{pmatrix} \partial a_{+\mu}/\partial \tau \\ \partial a_{-\mu}^*/\partial \tau \end{pmatrix} = \underbrace{\begin{pmatrix} -[1 + i\zeta_\mu - 2i|a_0|^2] & ia_0^2 \\ -ia_0^{*2} & -[1 - i\zeta_\mu + 2i|a_0|^2] \end{pmatrix}}_{=:M} \cdot \begin{pmatrix} a_{+\mu} \\ a_{-\mu}^* \end{pmatrix}, \tag{A.21}$$

with the corresponding eigenvalues λ of M:

$$\lambda = -1 \pm \sqrt{|a_0|^4 - (\zeta_\mu - 2|a_0|^2)^2}. \tag{A.22}$$

A.2.3 Nonlinear resonance shift, effective detuning and optical bistability

When using eq. A.19 to describe the dependence of the intracavity power $|a_0|^2$ on the pump laser detuning ζ_0 we find a Lorentzian resonance shape for small pump powers f^2 (in agreement with eq. A.7). However, when the pump laser power is increased, the resonance shape becomes asymmetric and eventually reaches the bistable regime where two stable values of intracavity power are possible at a given laser detuning. This is visualized in Figure A.1. Which solution is realized depends on the tuning direction of pump laser. When approaching the resonance from higher optical frequencies ($\zeta_0 < 0$) the 'upper branch' solution is realized; in the opposite scan direction the 'lower branch' solution describes the system. Experimentally the transmission trace corresponds to either a triangular resonance shape or an apparently narrowed resonance depending on the laser scan direction. Note that this effect is fully analogous to the thermal triangle described in Section 1.3.3. The pump laser tuning direction used for comb generation from high to low optical frequencies is indicated in Figure A.1. The maximal intracavity power of $|a_0|^2 = f^2$ is reached for an effective zero detuning (cf. Section 1.3.3) when the pump laser frequency is equal to the effective nonlinearly shifted resonance frequency. Below, in Section A.2.4 we will find $|a_0| = 1$ as an important threshold value for comb generation. In this context we note that this threshold is always reached as long as $f^2 \geq 1$ and that the pump laser detuning for reaching the threshold is always $\zeta_0 \leq 1$.
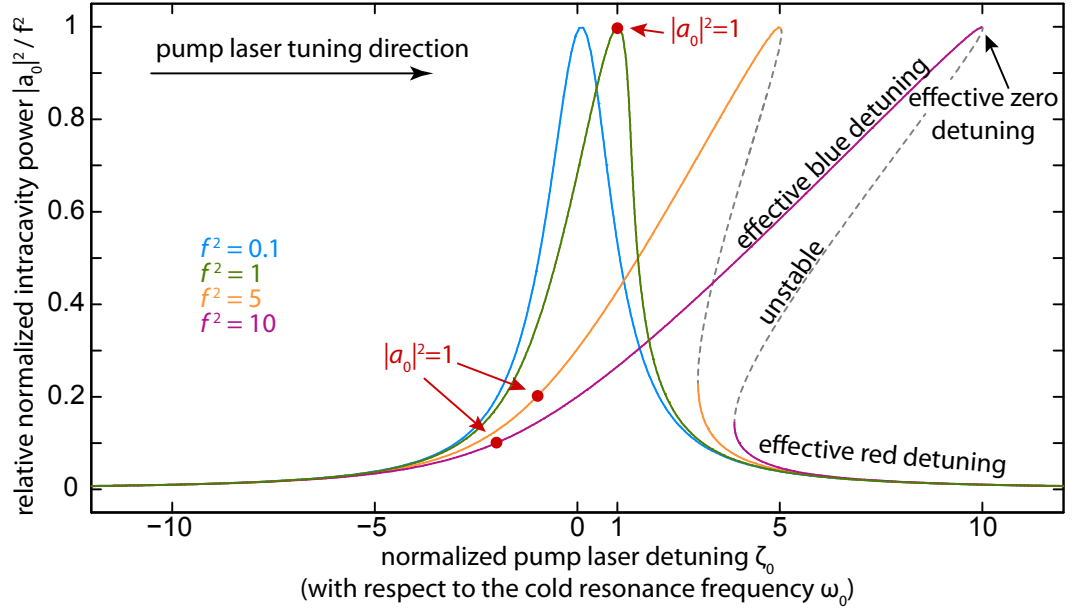
Figure A.1: Intracavity power vs. pump laser detuning: The normalized intracavity power $|a_0|^2/f^2$ is shown as a function of laser detuning $\zeta_0 = 2(\omega_0 - \omega_\mathrm{p})/\kappa$. For low pump powers ($f = 0.1$) the intracavity power follows a Lorentzian resonance shape. For higher pump powers the resonance becomes increasingly asymmetric due to the non-linear resonance shift (self-phase modulation). Eventually this leads to bistability, that this, two stable solutions for $|a_0|^2$ exist for a certain detuning values ζ_0. When tuning the pump laser ω_p into the resonance from the higher frequency side maximal intracavity power $|a_0|^2 = f^2$ is reached for an effective zero detuning when the pump laser frequency is equal to the effective nonlinearly shifted resonance frequency. Before (after) this point the pump laser is effectively blue (red) detuned. Tuning the laser beyond effective zero detuning results in a sudden jump to the lower branch solution causing a triangular resonance shape. The value value $|a_0|^2 = 1$ can always be reached for pump powers $f^2 \geq 1$ and a detuning of $\zeta_0 \leq 1$.

A.2.4 Threshold pump power

The expression $G = \Re(\lambda + 1)\kappa$ denotes the parametric gain[71] (in not normalized units) of the sidebands $+\mu$ and $-\mu$ that are excited if $G > \kappa$:

$$G = \sqrt{\kappa^2|a_0|^4 - 4(\omega_0 - \omega_p + \mu^2 D_2 - \kappa|a_0|^2)^2},$$
(A.23)

An illustration of the parametric gain lobes is shown in Fig. A.2a. To derive the threshold power (minimal pump power P_{in} for the generation of sidebands) we consider the maximal gain for the modes $\pm\mu$ where the second term under the radicand is close to zero. In the presence of (at least locally) anomalous dispersion (corresponding to $D_2, d_2 > 0$) this maximum can be reached approximately for some integer value of μ if D_2 is not too large[a]. We thus find that the minimal power required for $G > \kappa$ in the pump mode is $|a_0|^2 = 1$. Interestingly, this threshold power corresponds to a non-linear resonance shift of the pump mode of half a cavity linewidth. In not normalized units the intracavity threshold power can be written as

$$P_{\text{cav}}^{\text{th}} = \frac{\kappa}{2g T_R} = \frac{\kappa n_0^3 A_{\text{eff}}}{2\omega_0 n_2}.$$
(A.24)

To derive the threshold pump power, that is the minimal power in the coupling waveguide required to generate sidebands we can simply use assume the case of effective zero detuning where $|a_0|^2$ becomes maximal (effective nonlinear resonance frequency and laser frequency are both detuned from the cold resonance frequency towards smaller frequency by $\kappa/2$). Mathematically this corresponds to $\zeta_0 = 1$. Using $|a_0|^2 = 1$, $\zeta_0 = 1$ and eq. A.19 we find the threshold pump power required for the generation of parametric sidebands to be $f^2 = 1$ (also see ref.[141,142]) or equivalently in not normalized units:

$$P_{\text{in}}^{\text{th}} = \frac{\kappa^2 n_0^2 V_{\text{eff}}}{8\eta\omega_0 c n_2}$$
(A.25)

A.2.5 Emergence of the first mode

Here we address the question how distant (in terms of mode number difference) the first parametrically generated modes are with respect to the pump mode. We treat the general case where the pump power P_{in} can be higher than $P_{\text{in}}^{\text{th}}$. From the steady state eq. (A.19) the laser detuning can be expressed as a function of normalized energy

---

[a] This derivation assumes that the maximum gain can be reached for an integer value of μ. For high values of D_2 (typically reached in resonator with large FSR) this assumption may not be true and the gain maximum does not necessarily coincide with an integer value of μ (i.e. the spectral maximum of the gain does not coincide with a resonance frequency). In this case the effective threshold power computed below slightly underestimates the true threshold power.

in the pumped mode and the pump power. Here we make use of the fact that for $P_{in} \geq P_{in}^{th}$ (or equivalently $f^2 \geq 1$) the intracavity threshold power $|a_0|^2 = 1$ is always reached for a laser detuning $\zeta_0 \leq 1$ (cf. Section A.2.3):

$$\zeta_0 = |a_0|^2 - \sqrt{f^2/|a_0|^2 - 1}, \tag{A.26}$$

Using this, the definition of ζ_μ and eq. (A.23) at threshold (i.e. $G = \kappa$) we obtain

$$\sqrt{f^2/|a_0|^2 - 1} - d_2\mu_{th}^2 + |a_0|^2 - \sqrt{|a_0|^4 - 1} = 0. \tag{A.27}$$

Here, using the threshold power $|a_0|^2 = 1$, we find the relative mode number of the first sidebands at threshold

$$\mu_{th} = \sqrt{\frac{1}{d_2}(\sqrt{f^2 - 1} + 1)}. \tag{A.28}$$

Alternatively, this can be rewritten in SI units:

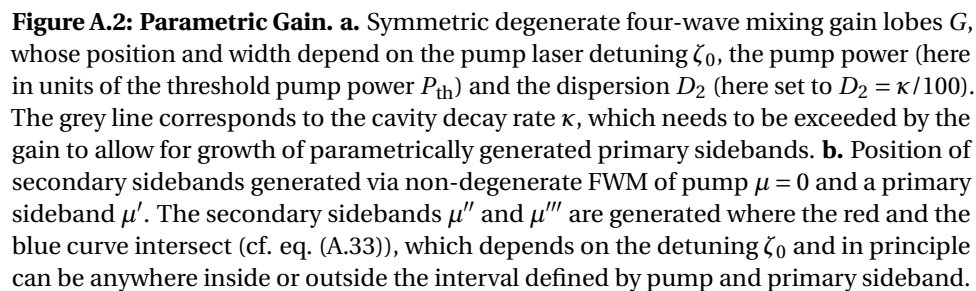$$\mu_{th} = \sqrt{\frac{\kappa}{D_2}\left(\sqrt{\frac{P_{in}}{P_{th}} - 1} + 1\right)} \tag{A.29}$$

The minimum obtainable μ_{th} is reached for $P_{in}^{th} = P_{in}$ only depends on the ratio of cavity decay κ rate to second order cavity dispersion D_2:

$$\mu_{th,min} = \sqrt{\frac{\kappa}{D_2}} \tag{A.30}$$

A.2.6 Emergence of secondary comb lines

In an analogous way we derive the relative mode numbers of the secondary sidebands μ'' and μ''' that emerge through a non-degenerate FWM process involving the pump $\mu = 0$ and a strong primary sideband μ'. Similar to before, we start from a linearized set of equations:

$$\frac{\partial a_{\mu''}}{\partial \tau} = -[1 + i\zeta_{\mu''} - 2i|a_0|^2 - 2i|a_{\mu'}|^2]a_{\mu''} + 2i a_0 a_{\mu'} a_{\mu'''}^*,$$
$$\frac{\partial a_{\mu'''}^*}{\partial \tau} = -[1 - i\zeta_{\mu'''} + 2i|a_0|^2 + 2i|a_{\mu'}|^2]a_{\mu'''}^* - 2i a_0^* a_{\mu'}^* a_{\mu''}. \tag{A.31}$$

Figure A.2: Parametric Gain. a. Symmetric degenerate four-wave mixing gain lobes G, whose position and width depend on the pump laser detuning ζ_0, the pump power (here in units of the threshold pump power P_{th}) and the dispersion D_2 (here set to $D_2 = \kappa/100$). The grey line corresponds to the cavity decay rate κ, which needs to be exceeded by the gain to allow for growth of parametrically generated primary sidebands. **b.** Position of secondary sidebands generated via non-degenerate FWM of pump $\mu = 0$ and a primary sideband μ'. The secondary sidebands μ'' and μ''' are generated where the red and the blue curve intersect (cf. eq. (A.33)), which depends on the detuning ζ_0 and in principle can be anywhere inside or outside the interval defined by pump and primary sideband.

where we neglect the influence of other excited lines, in particular the modes symmetric to the pump that are present even in the minimal configuration $(0, \pm\mu', \pm\mu'', \pm\mu''')$.

As before, we derive the eigenvalues for the system of equations A.31:

$$\lambda = -1 - \frac{i}{2}(\zeta_{\mu''} - \zeta_{\mu'''})$$
$$\pm 2\sqrt{|a_0|^2|a_\mu|^2 - (|a_0|^2 + |a_\mu|^2 - (\zeta_{\mu''} + \zeta_{\mu'''})/4)^2} \qquad (A.32)$$

The maximum gain value is reached when the second term in the radicand is zero, that is $(\zeta_{\mu''} + \zeta_{\mu'''})/4 = |a_0|^2 + |a_\mu|^2$. In this case, to overcome the cavity decay rate the product of the pump mode power and the power in the sideband needs to be $2\sqrt{|a_0|^2|a_\mu|^2} > 1$ implying $|a_0|^2|a_\mu|^2 > 1/4$. This yields:

$$\mu''^2 + (\mu' - \mu'')^2 = \frac{4(|a_0|^2 + |a_\mu|^2) + 2|\zeta_0|}{d_2} \qquad (A.33)$$

Fig. A.2b shows the left- and right-hand side of this expression as a function of relative mode number (For illustrative purposes we have set $|a_0|^2 + |a_\mu|^2) = 1$). The secondary sidebands are generated where the corresponding curves intersect. The location and number of intersection points depend on the pump laser detuning ζ_0. From Fig. A.2b it becomes clear that the secondary sidebands can be generated anywhere in between the two primary modes, and in principle also outside of the interval defined by pump and primary sideband.

Fig. A.3 shows typical examples of secondary sideband generation following previous primary sidebands generation. Experimentally a switching between different characteristic comb states (as shown in Fig. A.3a, b and c) may be observed when tuning into resonance.
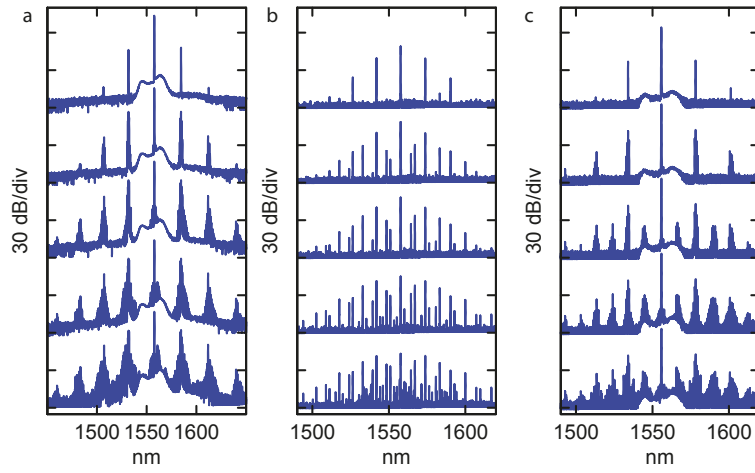
Figure A.3: Generation of primary and secondary sidebands following on prior generation of primary sidebands, observed in a 76 GHz FSR Si_3N_4 resonator. Secondary sidebands can either be generated **a.** close to the primary sidebands (pump power 2 W), **b.** isolated within the interval between primary lines (pump power 0.8 W), or **(c.)** in a combination of (a) and (b) (pump power 2 W).

B Noise consideration in a SiO$_2$ toroid

Chapter 2 presents an octave spanning spectrum generated directly in a fused silica microtoroid. In this spectrum, a broadening of the optical comb lines to ≈ 70 MHz is observed. This is much broader than the linewidth of the diode laser used for pumping. Here we will consider noise processes that have been studied in the past in the context of microresonators in order to understand if they can explain the observed noise phenomena in the microtoroid.

Any fluctuation in the parameters of the microresonator or the experimental conditions will affect the frequencies of the comb line. These fluctuations most prominently include changes in the resonance frequencies as well as amplitude and phase noise present in the pump laser and inside the cavity. Thus, a multitude of physical processes can account or contribute to the observation of broad comb lines. These processes include thermorefractive noise, thermoelastic noise, thermal Brownian motion, ponderomotive noise, photothermal noise, laser noise and self-/cross phase modulation.[5, 151–153] Phase noise can also be generated by optomechanical coupling[154–156] of optical and mechanical resonator modes, and by thermal oscillations of the resonator.[157]

Concerning the pump laser, we point out that any intensity noise $S_{PP}^{\text{in}}(\Omega)$ and phase noise $S_{\phi\phi}^{\text{in}}(\Omega)$ present in the pump laser transfers into intensity noise $S_{PP}^{\text{cav}}(\Omega)$ and phase noise $S_{\phi\phi}^{\text{cav}}(\Omega)$ inside the cavity (S_{PP} and $S_{\phi\phi}$ denote the noise spectral densities in units of rad^2/Hz and W^2/Hz). Using the standard quantum Langevin approach the transfer of noise into the cavity can be calculated.[198] Generally, fluctuations much faster in frequency Ω than the optical linewidth κ are filtered out and do not enter the cavity. For a critically coupled cavity and effective zero detuning $\omega_0^{\text{eff}} - \omega_{\text{p}} = 0$ (cf. Section 1.3.3) the intracavity intensity and phase noise is given by:

$$S_{PP}^{\text{cav}}(\Omega) = \frac{1/T_{\text{R}}^2}{(\kappa/2)^2 + \Omega^2} S_{PP}^{\text{in}}(\Omega) \tag{B.1}$$

$$S_{\phi\phi}^{\text{cav}}(\Omega) = \frac{(\kappa/2)^2}{(\kappa/2)^2 + \Omega^2} S_{\phi\phi}^{\text{in}}(\Omega) \tag{B.2}$$

It can be seen from eqs. B.1 and B.2 that for effective zero detuning there is no conversion between phase and intensity noise. In case of non-zero detuning, however, phase noise is converted to intensity noise and vice versa. For an effective detuning of $|\omega_0^{\text{eff}} - \omega_{\text{p}}| = \kappa/2$ the response to the pump noise of the critically coupled cavity is:

$$S_{PP}^{\text{cav}}(\Omega) = \frac{(\kappa^2 + \Omega^2)/T_{\text{R}}^2}{\kappa^4 + 4\Omega^4} S_{PP}^{\text{in}}(\Omega) + 4P_{\text{in}}^2 \frac{\Omega^2/T_{\text{R}}^2}{\kappa^4 + 4\Omega^4} S_{\phi\phi}^{\text{in}}(\Omega) \tag{B.3}$$

$$S_{\phi\phi}^{\text{cav}}(\Omega) = \frac{1}{4P_{\text{in}}^2} \frac{\kappa^2\Omega^2}{\kappa^4 + 4\Omega^4} S_{PP}^{\text{in}}(\Omega) + \frac{\kappa^2(\kappa^2 + \Omega^2)}{\kappa^4 + 4\Omega^4} S_{\phi\phi}^{\text{in}} \tag{B.4}$$

Here T_{R} is the cavity roundtrip time and P_{in} is the power in the coupling waveguide. The conversion from phase noise to noise is particularly relevant for diode pump lasers, such as the one used for octave spanning comb generation. In contrast to their amplitude noise, these lasers have significantly elevated phase noise.[199,200] The value of the root mean square (rms) power fluctuation δP_{cav} can be found by integrating S_{PP}^{cav} over the relevant frequency range according to

$$\delta P_{\text{cav}} = \left(\int S_{PP}^{\text{cav}}(\Omega) \frac{d\Omega}{2\pi} \right)^{1/2} . \tag{B.5}$$

Due to the complex interplay between the various noise mechanism it is difficult to estimate their magnitude quantitatively. The latter is even more difficult in the presence of the thermal and nonlinear lock (cf. Section 1.3.3) that will react on frequency and intensity fluctuation of the pump laser and cavity. Nevertheless, we will qualitatively describe processes that may contribute to the observed linewidth broadening Table B.1 list the parameters of the toroidal fused silica resonator that was employed for comb generation. We keep in mind that a resonance frequency ω_μ is changed by an amount $\delta\omega_\mu$ when the refractive index n or the cavity's radius R experience modifications δn or δR, respectively:

$$-\frac{\delta\omega_\mu}{\omega_\mu} = \frac{\delta n}{n} + \frac{\delta R}{R} \tag{B.6}$$

Parameter	Value
Radius R	$40\ \mu$m
Refractive index n_0	1.44
Non-linear effective mode area A_{eff}	$4\ \mu$m^2
Non-linear index n_2	$2.2 \times 10^{-20}\text{m}^2\text{W}^{-1}$
Cavity round trip time T_R	$2\pi R n/c \approx 1.2 \times 10^{-12}$ s
Optical linewidth $\kappa/(2\pi)$	10 MHz
Pump frequency ν_{pump}	193 THz
Pump power P_{in}	2 W
Resonator temperature T	1000 K
$(1/n)(\mathrm{d}n/\mathrm{d}T)$	$1 \times 10^{-5}\text{K}^{-1}$
$(1/R)(\mathrm{d}R/\mathrm{d}T)$	$5.5 \times 10^{-7}\text{K}^{-1}$
Material density ρ	2.2 g/cm^3
Specific heat capacity C	700 J kg^{-1}K^{-1}
Effective resonator mass m_{eff}	10 ng
Compressiblility β	2.7×10^{-11} Pa^{-1}

Table B.1: Toroid and experiment parameters of a microresonator and experimental conditions for estimating the expected comb frequency noise[98]

Thermodynamic fluctuations

The thermodynamic fluctuations of a small material volume V that is coupled to a thermal bath with temperature T can be expressed as independent root-mean-square fluctuation δT and δV of temperature and volume, respectively.[201] For a microresonator this translates into[153]

$$\delta T = \sqrt{\frac{k_B T^2}{C \rho V_{\text{eff}}}}, \tag{B.7}$$

$$\frac{\delta V_{\text{res}}}{V_{\text{res}}} = \sqrt{\frac{k_B \beta T}{V_{\text{res}}}}, \tag{B.8}$$

where V_{eff} is the mode volume and V_{res} the resonator volume. Furthermore, k_B denotes the Boltzmann constant, C the specific heat capacity, ρ the material density and β the material compressibility. As these fluctuations are larger for smaller volume they can become significant in microresonators. This is particularly true for fused SiO$_2$ toroidal microresonators that can reach high temperatures[5] up to 1000 K in their small mode volumina V_{eff}. The temperature fluctuation δT induces, both, modulation of the refractive index n and the radius R of the resonator via thermo-refractivity $\mathrm{d}n/\mathrm{d}T$ and thermal expansion $\mathrm{d}R/\mathrm{d}T$, respectively. The volume fluctuation affects the radius via $\delta R/R = 1/3 \cdot \delta V_{\text{res}}/V_{\text{res}}$. Note that the latter effect is independent of temperature fluctuations and may be interpreted as Brownian motion. From the above expressions

it can be seen that the fluctuation scale only linear and sub-linear with the temperature. Thus the fact that low noise combs with linewidth well below one MHz have been achieved in similar resonator geometries before at room temperature, implies that, even for high temperatures, thermodynamics fluctuations can not explain the observed linewidth broadening. While thermodynamics fluctuations pose a fundamental limit to the frequency stability of microresonators,[153] they are not responsible for the observed linewidth broadening.

Photothermal effects

Besides the thermodynamic temperature fluctuations, temperature fluctuations can also be caused by fluctuations in the absorbed power. If P_{abs} denotes the power that is absorbed in the cavity, then $N_{abs} = P_{abs} T_R / (\hbar \omega_p)$ is the number of absorbed photons. As absorption is a statistical process the fluctuation in the number of photons is given by $\delta N = \sqrt{N_{abs}}$, implying the fluctuation in the absorbed power of $\delta P_{abs} = \sqrt{\hbar \omega_p P_{abs} T_R}$. The noise S_{PP}^{cav} has a much smaller effect as it is drastically diminished by the low absorption coefficient in fused silica. Thus the temperature fluctuations induced by the pump laser can be estimated to

$$\delta T = \frac{\sqrt{\hbar \omega_p P_{abs} T_R}}{C \rho V} \tag{B.9}$$

Even when setting $P_{abs} = P_{in}$ the temperature fluctuation δT in the photothermal case is two orders of magnitude smaller compared to the case of thermodynamic temperature fluctuation. This implies that photothermal effects are not relevant for the present case.

Thermal oscillations

Another effect related to absorption of the pump light in the cavity are thermal oscillation, which can occur as a result of the finite response time of the thermal resonance shift to a change in intracavity power and the finite cavity build-up time.[157,185] These thermal oscillations, however, require a high material absorption in comparison to scattering induced losses; this criterion is not met in the present high-Q fused silica microtoroid.[157]

Self- and crossphase modulation

The Kerr nonlinearity converts fluctuations in the circulating power δP_{cav} to variations in the refractive index

$$\delta n = n_0 + n_2 \frac{\delta P_{\text{cav}}}{A_{\text{eff}}}, \qquad (B.10)$$

which in turn is responsible for changes in the resonance frequency. It is important to note that the different self- and cross-phase modulational frequency shift on pump mode and other resonator modes will cause a differential frequency shift (cf. Section 1.3.3). In the present case, where a diode laser was used as the pump laser, significant power variations δP_{cav} may be introduced to the cavity by conversion of the high diode laser phase noise $S_{\phi\phi}^{\text{in}}(\Omega)$ into cavity intensity noise $S_{PP}^{\text{cav}}(\Omega)$ according to eq. B.3. Note that for a detuned pump laser the resulting cavity phase noise via the above described mechanism can exceed the pump laser phase noise by several orders of magnitude. Given the phenomenological observation that the comb line broadening depends on the pump laser detuning, self- and cross phase modulation may be responsible for the observed broad comb lines.

Mechanical oscillations induced by radiation pressure

The high light intensities inside the resonator exert a radiation pressure force on the resonator's boundary. It has been shown that radiation pressure of the photons inside the resonator results in a coupling of optical to mechanical degrees of freedom in microtoroids.[202] Here, a blue detuned pump laser (which is the case for comb generation) can transfer photonic energy into mechanical energy and parametrically drive regenerative mechanical oscillations. These mechanical oscillations act back on the cavity resonance frequencies and could lead to a change of the comb lines frequencies. The threshold power for this so called opto-mechanical parametric instability scales with the effective mass of the mechanical oscillator m_{eff} and the mechanical damping rate[202]:

$$P_{\text{mech}}^{\text{th}} \sim m_{\text{eff}} \Gamma. \qquad (B.11)$$

While the comb generating toroid is fabricated in a way that ensures highest possible mechanical damping (small undercut, cf. Section 1.2.2) high-Q mechanical modes may still be present. To test the influence of parametric instabilities of the resonator an etched tungsten probe is used to increase the damping rate of mechanical modes. Figure B.1 shows a microscope image of the employed tungsten probe. The probe is moved across the resonator geometry, and in particular, as close to the optical mode as possible without preventing comb generation. In this measurements no

influence on the optical linewidth of comb modes has been observed. While therefore unlikely, parametric instability can not be fully ruled out. Moreover, it has been shown that the radiation pressure induced coupling between optical and mechnaical modes can lead to a chaotic chaotic quivering of the resonator[159] at high pump powers. Optomechanical effects could therefore contribute to the observed noise, in particular as the frequency noise due to chaotic optomechanical dynamics extends to high Fourier frequency > 10 MHz.[159]
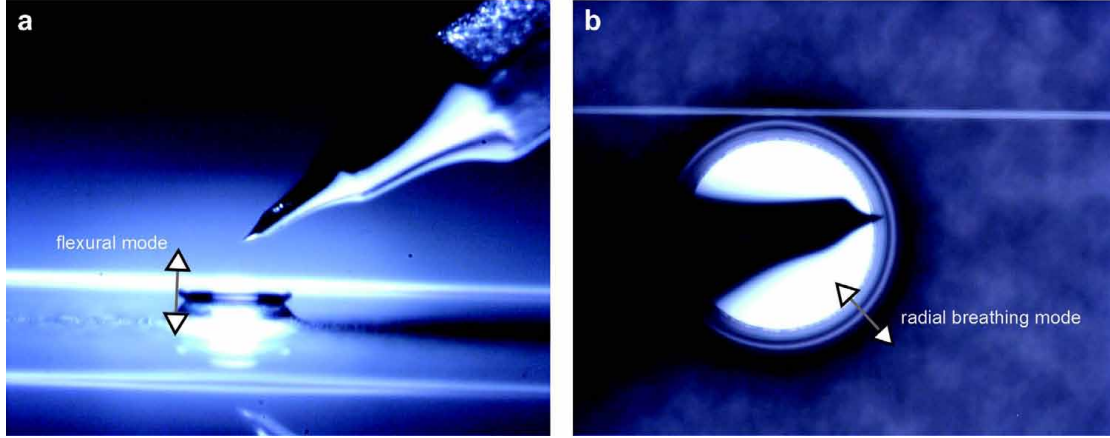
Figure B.1: Etched tungsten probe for quenching mechanical oscillations of a micro-toroid. **a**. Side view of the tungsten probe. **b**. Top view of the probe in contact with the resonator close to the toroid rim. The resonator diameter is 80 μm. The mechanical flexural and radial breathing modes are illustrated by arrows in the direction of the mechanical displacement.

C Theory of temporal dissipative solitons in microresonators

C.1 Analytical description of solitons in a microresonators

To describe the internal field in a nonlinear microresonator the Nonlinear Schrödinger Equation (NLS) may be used when third and higher order dispersion terms are neglected[191]:

$$\frac{\partial A}{\partial t} - i\frac{1}{2}D_2\frac{\partial^2 A}{\partial \phi^2} - ig|A|^2 A = -\left(\frac{\kappa}{2} + i(\omega_0 - \omega_p)\right)A + \sqrt{\frac{\kappa\eta P_{\text{in}}}{\hbar\omega_0}}. \tag{C.1}$$

Here $A(\phi, t) = \sum_\mu A_\mu e^{i\mu\phi - i(\omega_\mu - \omega_p)t}$ is the slowly varying field amplitude and ϕ is the angular coordinate inside the resonator. This equation may be obtained from the nonlinear equation for the slowly varying amplitude in time domain by using the substitution:

$$\omega_\mu = \omega_0 + D_1\mu + \frac{1}{2}D_2\mu^2 = \omega_0 + D_1\mu - \frac{1}{2}D_2\frac{\partial^2}{\partial\phi^2}, \tag{C.2}$$

as $\sum_\mu(i\mu)^n A_\mu e^{i\mu\phi - i(\omega_\mu - \omega_p)t} = F.T.\left[\frac{\partial^n}{\partial\phi^n}A(\phi, t)\right]$ (details of analogous derivation for a fiber are given by Boyd[135]).

Transforming eq. (C.1) to its dimensionless form gives:

$$i\frac{\partial \Psi}{\partial \tau} + \frac{1}{2}\frac{\partial^2 \Psi}{\partial \theta^2} + |\Psi|^2\Psi = (-i + \zeta_0)\Psi + if. \tag{C.3}$$

Here $\theta = \phi\sqrt{\frac{1}{2d_2}}$ is the dimensionless longitudinal coordinate, $\Psi(\tau, \phi) = \sum A_\mu(\tau)e^{i\mu\phi}$ is the waveform, and $d_2 = D_2/\kappa$ is the dimensionless dispersion. Equation (C.3) is identical to the Lugiato-Lefever equation,[182] where a transversal coordinate is used instead of a longitudinal one in our case. Using the ansatz of a stationary ($\frac{\partial \Psi}{\partial \tau} = 0$)

soliton on a continuous-wave (cw) background[180] we find an expression for a single soliton

$$\Psi = \Psi_0 + \Psi_1 \simeq \Psi_0 + Be^{i\varphi_0}\mathrm{sech}(B\theta), \tag{C.4}$$

where the real number B defines both, width and amplitude of the soliton and φ_0 defines the phase angle. We note that eq. (C.4) is not an exact solution of eq. (C.3), for which exact soliton solutions are known only in the case of zero losses.[186]

The constant cw background Ψ_0 can be found by inserting Ψ_0 into eq. (C.3) as the lowest branch[186] of the solution of

$$(|\Psi_0|^2 - \zeta_0 + i)\Psi_0 = if, \tag{C.5}$$

which, eventually, results when $\zeta_0 > \sqrt{3}$ (bistability criterion) and large enough detunings $f^2 < \frac{2}{27}\zeta_0(\zeta_0^2 + 9)$ in:

$$|\Psi_0|^2 = \frac{2}{3}\zeta_0 - \frac{2}{3}\sqrt{\zeta_0^2 - 3}\cosh\left(\frac{1}{3}\,\mathrm{arcosh}\left(\frac{2\zeta_0^2 + 18\zeta_0 - 27f^2}{2(\zeta_0^2 - 3)^{2/3}}\right)\right),$$

$$\Psi_0 = \frac{if}{|\Psi_0|^2 - \zeta_0 + i} \simeq \frac{f}{\zeta_0^2} - i\frac{f}{\zeta_0}. \tag{C.6}$$

The soliton component Ψ_1 in eq. (C.4) is approximated by the bright soliton solution of the ordinary NLS (no damping, no driving), which is the limit case for $\zeta_0 \gg 1$.

The parameters B and φ_0 can be derived based on general conditions for the soliton attractor,[180] which yields

$$B \simeq \sqrt{2\zeta_0}, \tag{C.7}$$

$$\cos(\varphi_0) \simeq \frac{\sqrt{8\zeta_0}}{\pi f}. \tag{C.8}$$

Based on eqs. (C.6,C.7) we can estimate the ratio R of soliton peak power to cw pump background:

$$R = \frac{|B|^2}{|\Psi_0|^2} = \frac{2\zeta_0^3}{f^2}. \tag{C.9}$$

For a maximal detuning $\zeta_0 = \zeta_0^{\max}$ (see eq. (C.13) below) we find:

$$R_{\max} = \frac{\pi^6 f^4}{2^8} = \left(\frac{\pi^3 g\eta P_{\mathrm{in}}}{2\kappa^2 \hbar\omega_0}\right)^2. \tag{C.10}$$

Extending eq. (C.4) to the case of multiple solitons inside the resonator gives

$$\Psi(\phi) \simeq \underbrace{\Psi_0}_{C_1} + \underbrace{\left(\frac{4\zeta_0}{\pi f} + i\sqrt{2\zeta_0 - \frac{16\zeta_0^2}{\pi^2 f^2}}\right)}_{C_2} \sum_{j=1}^{N} \text{sech}(\sqrt{\frac{\zeta_0}{d_2}}(\phi - \phi_j)). \tag{C.11}$$

It was shown[180] that if a pair of solitons in a train is separated by a distance $\phi_{j+1} - \phi_j \gtrsim (8/B)\sqrt{2d_2}$ the pair of solitons does not interact. This puts a possible limit $N_{\max} < \frac{2\pi}{8}\sqrt{\zeta_0/d_2}$ of a maximum number of stationary solitons in the resonator and consequently the maximum number of "steps" in intracavity power and transmission. Assuming that soliton can only emerge for $\zeta_0 > \sqrt{3}$ (bistability criterion), we find $N_{\max} \approx \sqrt{\kappa/D_2}$, which remarkably coincides with the distance between the first generated primary sidebands $\mu_{\text{th,min}}$ in the process of comb generation.[3]

C.2 Limit conditions for solitons in microresonators

By substituting $|h| = |f|/\sqrt{2\zeta_0^3}$, $\gamma = 1/\zeta_0$, $\tilde{\theta} = \sqrt{2\zeta_0}\theta$, $\Psi = \sqrt{2\zeta_0}\tilde{\Psi}$ and changing the phase of the pump, (C.3) is transformed to the damped driven NLS equation for the stationary case:

$$\frac{\partial^2 \tilde{\Psi}}{\partial \tilde{\theta}^2} + 2|\tilde{\Psi}|^2\tilde{\Psi} - \tilde{\Psi} = -i\gamma\tilde{\Psi} - h, \tag{C.12}$$

which was analyzed for infinite boundary conditions by Barashenkov et al.[186] In particular the condition for the soliton existence $h > 2\gamma/\pi$ transforms into:

$$\zeta_0^{\max} = \pi^2 f^2/8. \tag{C.13}$$

Eq. (C.13) can also be found from the requirement that the right part in equation (C.8) must be smaller than unity. In[186] it was further shown analytically that the boundaries separating the regimes of existence of solitons (as described in the main text) are defined by characteristic curves for $\tilde{\Psi}_0$ in (C.12). In our case this translates into

$$|\Psi|_{\pm}^2 = \frac{2}{3}\zeta_0 \pm \frac{1}{3}\sqrt{\zeta_0^2 - 3} \tag{C.14}$$

Numerical simulations for our system with periodic boundary conditions show that all these limits remain valid with very good quantitative agreement for a sufficiently large number $K \gg \frac{2}{\pi}\sqrt{\frac{\zeta_0^{\max}}{d_2}} = f\mu_{\text{th,min}}/\sqrt{2}$ of modes (typically a few hundreds).

C.3   Analytical description of steps in the intracavity power

The height of steps in the intracavity power can be found by averaging the waveform amplitude (eq. C.11) squared over one roundtrip for different numbers N of solitons:

$$\overline{|\Psi|^2} = |\Psi_0|^2 + N \cdot \xi(K) \frac{1}{2\pi} \int_0^{2\pi} (\Psi_1^2 + \Psi_0 \Psi_1^* + \Psi_1 \Psi_0^*) d\phi$$

$$= |\Psi_0|^2 + N\sqrt{2d_2}(\Psi_0' \cos\phi_0 + \Psi_0'' \sin\phi_0 + \sqrt{2\zeta_0}/\pi) \simeq \frac{f^2}{\zeta_0^2} + N\xi(K)\frac{2}{\pi}\sqrt{d_2\zeta_0}.$$

$$(C.15)$$

As shown in Fig. 3 in the main manuscript, this approach also describes the laser tuning dependence of the step height. When comparing to the numerical simulations with a rather low mode number, we use a correction factor $\xi(K)$ of order unity ($\xi(K) \simeq$ 1.3 in the case of 101 simulated modes). For a higher number of simulated modes (e.g. 501) this correction is not required (cf. comment in sec. C.2).

C.4   Optical spectrum and temporal width of solitons in a micro- resonator

The optical spectrum $\Psi(\mu)$ of the soliton has the same hyperbolic secant form as the time domain waveform. Mathematically this corresponds to the Fourier transform of a hyperbolic secant being again a hyperbolic secant:

$$\Psi(\mu) = \text{F.T.}\left[\sqrt{2\zeta_0}\,\text{sech}\left(\sqrt{\frac{\zeta_0}{d_2}}\phi\right)\right] = \sqrt{d_2/2}\,\text{sech}\left(\frac{\pi\mu}{2}\sqrt{\frac{d_2}{\zeta_0}}\right). \qquad (C.16)$$

Using the relation for the optical frequency $\omega = \omega_p + \mu D_1$ and the time $t = \frac{\phi}{2\pi} T_R = \phi/D_1$ spectral envelopes and the soliton waveform can be rewritten:

$$\Psi(\omega - \omega_p) = \sqrt{d_2/2}\,\text{sech}((\omega - \omega_p)/\Delta\omega) \ \text{ with } \Delta\omega = \frac{2D_1}{\pi}\sqrt{\frac{\zeta_0}{d_2}}. \qquad (C.17)$$

and

$$\Psi(t) = \sqrt{2\zeta_0}\,\text{sech}(t/\Delta t), \ \text{ with } \Delta t = \frac{1}{D_1}\sqrt{\frac{d_2}{\zeta_0}}. \qquad (C.18)$$

The minimal achievable soliton duration can be found by using $\zeta_0^{\max}$ (eq. C.13) in the above equation for Δt:

$$\Delta t_{\min} = \frac{1}{\pi D_1} \sqrt{\frac{\kappa D_2 n_0^2 V_{\text{eff}}}{\eta P_{\text{in}} \omega_0 c n_2}}. \tag{C.19}$$

This equation can be recast in terms of the group velocity dispersion $\beta_2 = \frac{-n_0}{c} D_2 / D_1^2$, the nonlinear parameter $\gamma = \frac{\omega}{c} \frac{n_2}{A_{\text{eff}}}$ (for simplicity we assume critical coupling $\eta = 1/2$ and on resonant pumping):

$$\Delta t_{\min} = \frac{2}{\sqrt{\pi}} \sqrt{\frac{-\beta_2}{\gamma F P_{\text{in}}}}, \tag{C.20}$$

where denotes the finesse $F = \frac{D_1}{\kappa}$ of the cavity. Note that the values $\Delta\omega$ and Δt need to be multiplied by a factor of $2\,\text{arccosh}(\sqrt{2}) = 1.763$ to yield the FWHM of the sech^2-shaped power spectrum and pulse intensity, respectively.

For the time bandwidth product (TBP) we find $\Delta t \Delta\omega = 2/\pi$ or, when considering the FWHM of spectral and temporal power (in units of Hz and s), TBP = 0.315.

C.5 Soliton mode-locking in lasers vs. soliton formation in micro-resonators

This section compares soliton formation in microresonators with soliton mode-locking in lasers where a saturable absorber is necessary for soliton stability:

Soliton mode-locking in lasers: Generally mode-locking requires a pulse shaping mechanism, which can be achieved in different ways for example via a fast saturable absorber that forms the circulating intensity inside the laser cavity into a pulse.[45] Here, the shortest achievable pulse duration is limited by the relaxation time of the fast saturable absorber. Another mode-locking mechanism is soliton mode-locking, where the pulse shaping mechanism is provided by the formation of solitons in the presence of negative group velocity dispersion and self-phase modulation via the cavity's non-linearity. This method is widely used and well understood in the context of mode-locked laser and ultra-short optical pulse generation.[51,203] While the pulse shaping does not rely on the effect of a saturable absorber, it has been shown theoretically and experimentally that soliton mode-locked lasers still require a saturable absorber, which ensures the stability of the soliton against the growth of a narrow-bandwidth cw background.[51,203] This cw background arises from the interaction and reshaping of the soliton in the laser cavity and subsequently experiences a larger gain as the soliton, which due to its broadband spectral nature falls into the outer, lower

gain parts of the spectral laser gain window. It is important to note that in the case of soliton mode-locking the relaxation time of the saturable absorber does not limit the achievable pulse duration; it merely ensures the suppression of the continuum on intermediate timescales.[204]

Soliton formation in microresonators: Soliton formation in microresonators is similar to soliton mode-locking in lasers. As in the case of a soliton-mode locked laser solitons are formed due to a balance between cavity nonlinearity and self-phase modulation. However, while microresonators are driven by a continuous wave pump laser they are not lasers. The conversion of the continuous pump laser light into other frequency components and the amplification of the newly generated frequency components rely exclusively on the parametric gain due to the Kerr-nonlinearity of the resonator material. The cw pump laser coincides directly with a spectral component of the solition. Importantly, a saturable absorber is not required for the stability of the solitons as detailed below: Mathematically the coherently driven, damped Kerr-nonlinear microresonator is described by the Lugiato-Lefever equation,[182] which is identical to a damped, driven nonlinear Schrödinger equation. Dissipative temporal cavity solitons, superimposed onto a weak continuous wave background, have been proven to exist as stable mathematical solutions to this equation.[180] Due to the cavity loss, these solitons are dissipative in their nature and their persistence requires a source of energy for replenishment. The latter is provided by continuously and coherently driving the cavity.

The continuous wave background on which the solitons exist in the case of a microresonator is very different from the detrimental cw background in a soliton mode-locked lasers. It is a coherent internal field originating from the pump laser. It is not a narrow bandwidth low intensity cw background pulse produced by perturbation of the soliton. As opposed to a spectrally limited but continuous laser gain medium (continuous in the sense that it can amplify any frequency component within the gain bandwidth) the parametric gain profile is highly frequency selective (as energy conservation needs to be fulfilled in the frequency conversion processes). Moreover, the parametric gain profile depends on the light frequencies and intensities present in the cavity and relies on the phase coherent interaction between all these light frequencies. While it cannot replace a stringent mathematical stability analysis as mentioned above, this illustrates that the growth of a destabilizing cw background is generally not supported in a microresonator. Hence, stable soliton formation in a microresonator does not require a saturable absorber and the solitons are well described by the Lugiato-Lefever equation. This also is in perfect agreement with our experiments, which reveal the generation of stable solitons in optical microresonators.

D Experimental methods

D.1 Frequency comb calibrated broadband laser scan

D.1.1 Setup and principle

Frequency comb calibrated broadband (multi-THz) laser scans[84] are a powerful tool to combine the broadband tuning characteristics of diode lasers and the frequency accuracy of an mode-locked fiber laser comb. In this work frequency comb calibrated laser scans are used for measuring resonator dispersion and for performing the frequency reconstruction of microresonator based combs.

First, it is described how the diode laser scan is calibrated. The experimental setup is shown in Figure D.1. The diode laser light is split into two calibration beams: The
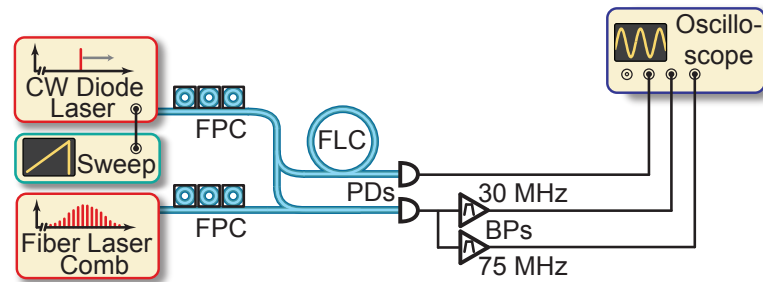
Figure D.1: Setup for frequnecy comb calibrated laser scans. A cw diode laser performs a voltage controlled scan over a multi-THz bandwidth. A fiber loop cavity (FLC) and a fiber laser comb are used to provide a frequency calibration for the laser scan. FPC: Fiber polarization controller; PD: photodetector; BP: Bandpass filter.

first beam is combined with the spectrum of a conventional(commercial) mode-locked fiber laser comb (repetition rate $f_{\text{rep}} = 250$ MHz, see Figure 1.1a for a typical spectrum) resulting in a heterodyne beatnote between the fiber laser comb and the scanning diode laser. Here, we only consider the lowest frequency beatnote ≤ 125 MHz

corresponding to the frequency distance between diode laser and nearest comb line. As illustrated in Figure D.2a the heterodyne beatnote (detected by a photodetector) linearly ramps back and forth between zero and $f_{rep}/2 = 125$ MHz. Two RF bandpath filters at frequencies 30 MHz amd 75 MHz (bandwidth 1 MHz) are used to filter the beatnote signal. This results in electronic marker signals, whenever the scanning diode laser is reaching a frequency that is 30 MHz or 75 MHz above or below the nearest comb line frequency (cf. Figure D.2b). The two electronic marker signals resulting from the filtering at 30 MHz and 75 MHz are recorded simultaneously on separate channels of a oscilloscope (10 million sampling points, peak detect mode). A schematic example of the recorded marker signals as a function of scan time is shown in Figure D.2c. The frequency calibration of the laser scan, that is mapping the time in the scan onto a relative laser frequency detuning is done in a post-processing step. The characteristic pattern of the four electronic markers around each comb line allows to assign a relative detuning to all recorded markers. Interpolating this detuning between adjacent markers allows to assign a relative laser detuning to all times during the scan.

The **second beam** is coupled to a fiber-loop cavity (FLC) with a FSR of ~ 10 MHz and the transmission is recorded simultaneously on another oscilloscope channel. The FLC transmission signal creates a fine ruler of transmission dips that can further increase the accuracy of the laser scan - in particular, when the laser scan velocity is changing between two comb line markers. Nnote that the signal is inverted to yield peaks instead of dips in the recorded trace. The FSR of the FLC is subject to dispersion and slightly changing over the bandwidth of the laser scan. It can be locally calibrated using the frequency comb markers. A typical calibration data set is shown in Figure D.3. The scan bandwidth is limited by the diode laser range on one side, and by the spectral span of the fiber-laser comb on the other. More than 10000 electronic markers and more than 70000 FLC resonances are recorded in a single scan.

D.1.2 Data post-processing

First, a peak-detection algorithm is used to find the positions of the comb calibration markers and FLC resonances as illustrated in Figure D.3b and Figure D.3c. The algorithm assumes a minimal separation between adjacent peaks. The detected horizontal peak position is refined by using the mean position of the rising and falling edge at half maximum height.

Second, the consistency of the detected markers is checked. Any deviation from the regular pattern (..., 75 MHz marker, 30 MHz marker, 30 MHz marker, 75 MHz marker, ...) indicates an deviation from a steady and monotonic laser scan (cf. Figure D.4a). It can in addition be tested, whether the number of FLC resonances between two comb
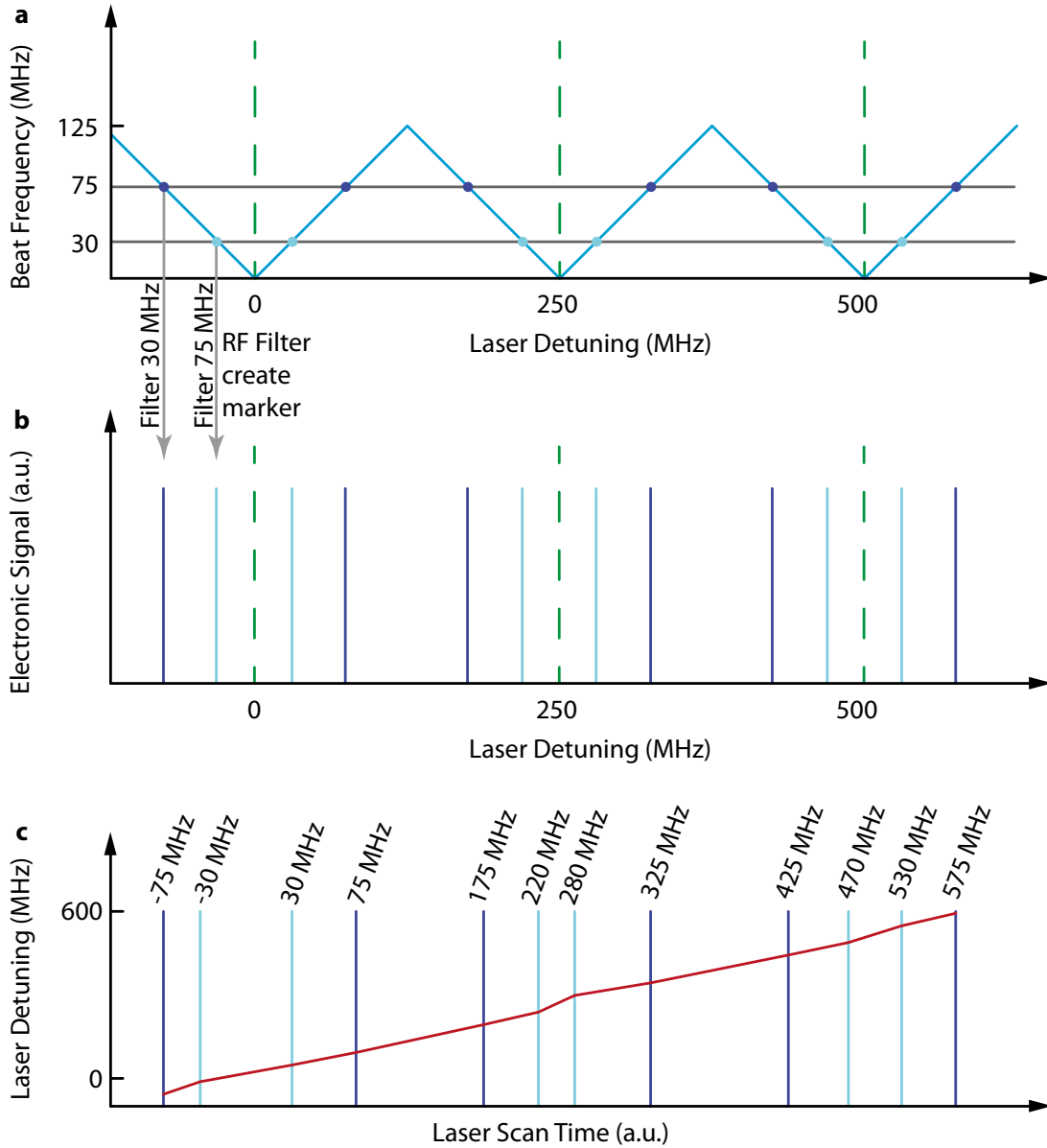
Figure D.2: Frequency calibration using a frequency comb. a. Heterodyne beatnote frequency (light blue) between diode laser and neares comb line (dashed green). **b.** The detected and electronically bandpass filtered (at 30 MHz and 75 MHz) heterodyne beat-note yields electronic calibration marker when the laser is frequency offset from a comb line by either 30 MHz or 75 MHz. **c.** Illustration of a typical data set where calibration markers are recorded as a function of scan time. The characteristic pattern of the markers allows to determine their relative laser detuning frequency (labels). Interpolation results in frequency calibration for all any point in time during the scan (red curve).
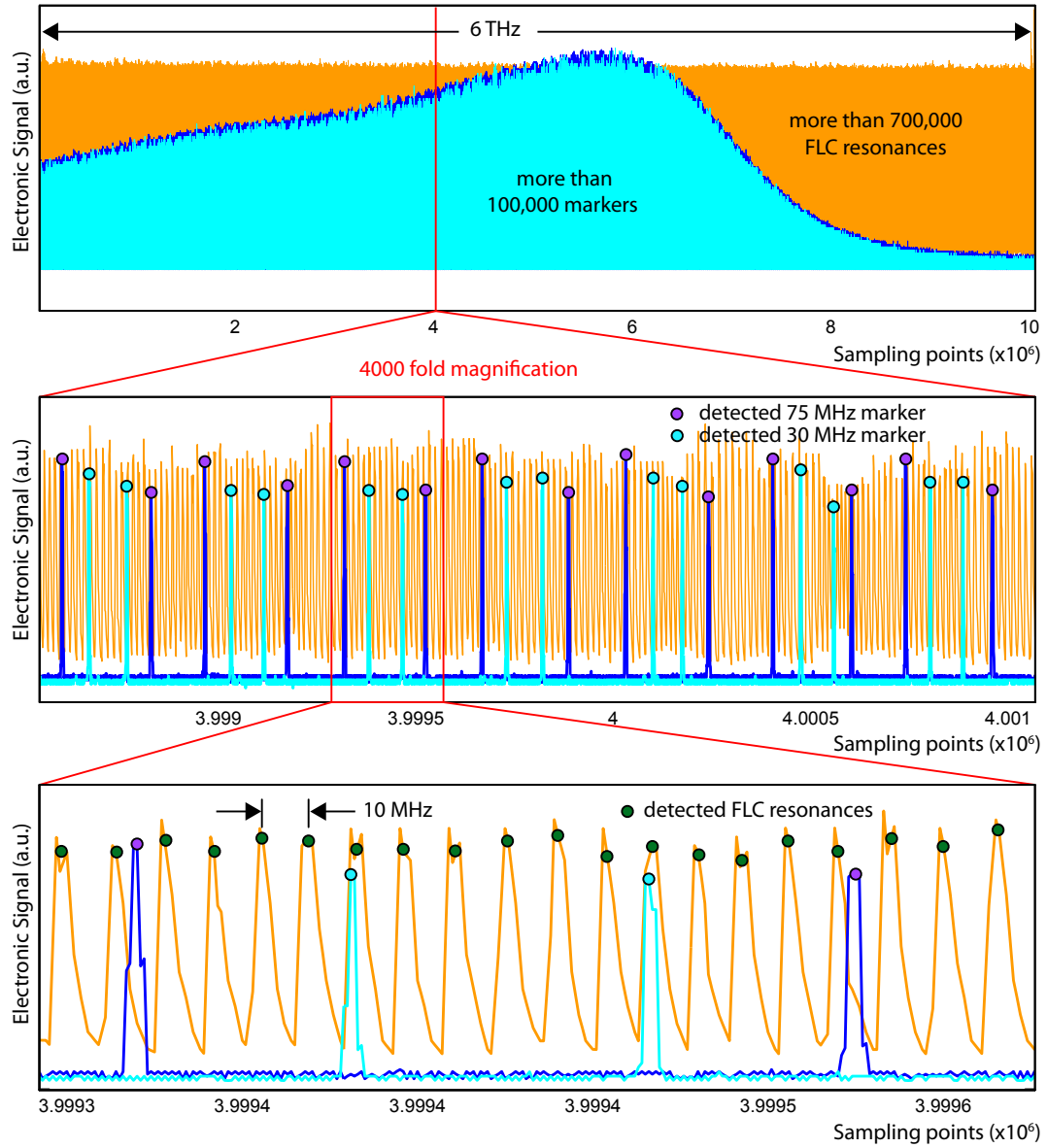
137

Figure D.3: Experimental calibration data. The data comprise two types of comb line markers resulting from the bandpass filtering at 30 MHz (light blue) and 75 MHz (dark blue), as well as, the fiber loop cavity (FLC) transmission (inverted, resonances are peaks). The colored dots mark the automatically detected peaks, which serve as a basis for the frequency calibration.

markers is consistent with the FSR of the FLC (cf. Figure D.4b).

Third, a relative laser detuning is assigned to all markers and via interpolation to all sampling points (corresponding to the time in the scan). The accuracy can be further increased by employing the finer FLC grid.
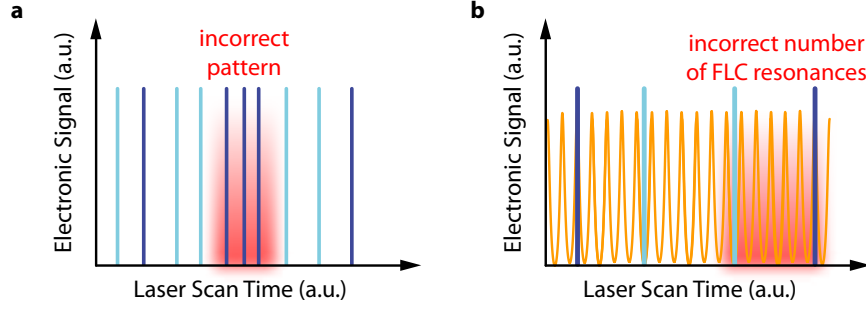

Figure D.4: Scan error detection. (same colorcode as in Figure D.3) **a.** Inconsistency in the marker pattern indicating an unsteady or not monotonic laser scan. **b.** The locally calibrated FSR of the fiber loop cavity (FLC) allows a consistency check between comb line markers and may reveal otherwise undetected scan errors on much finer scale than in (a).

D.1.3   Limitation of the method

In principle the described method allow for sub-MHz resolution over a scan bandwith of several THz. In broadband scans the precision of the method is limited by the number of available sampling points (note: the peak detect mode reduces the effective number of sampling point by a factor of two) and frequency jitter of the diode laser. The combined effect can be estimated when determining the FSR of the FLC based on individual adjacent peaks of the FLC transmission trace as shown in Figure D.5. A frequency jitter of several MHz is observable. The exact value depends on the diode laser head parameters, namely, temperature and current as well as scan parameters such as wavelength range and scan speed. In terms of spectral scan bandwidth the method is limited by the mode-hop free tuning range of the laser and the spectral coverage of the underlying fiber laser calibration comb.

D.1.4   Measurement of resonator dispersion and comb reconstruction

Measurement of resonator dispersion

For dispersion measurement (requiring knowledge of the relative frequencies of the microcavity resonances) another fraction of the scanning diode laser is used to probe
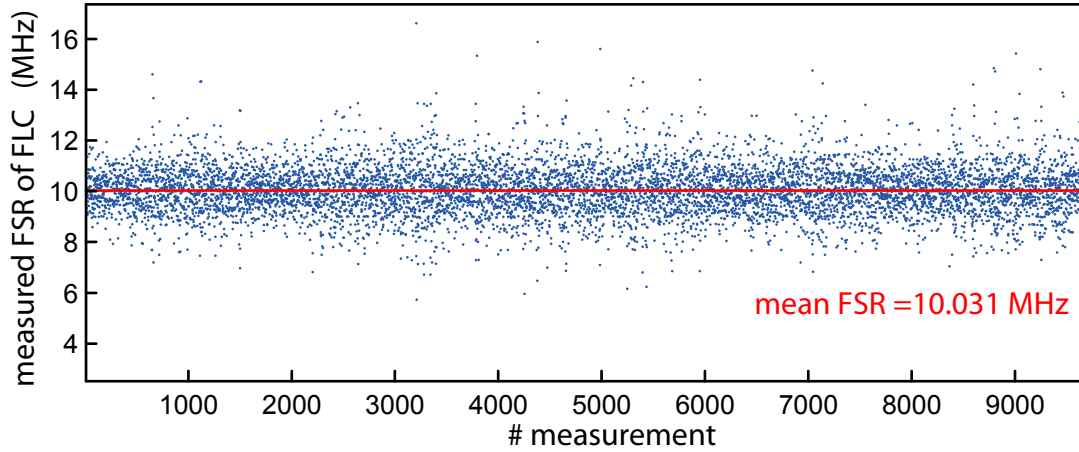
Figure D.5: Free spectral range of the Fiber loop cavity. Using only the frequnecy comb markers as a calibration the difference between adjacent fiber loop cavity (FLC) resonances is determined for approximately 10000 resonances in the central area of the scan. The local FSR is 10.031 MHz. The individual measurements show a few MHz scatter around the mean value which is mainly due to frequency jitter in the scanning diode laser and the limited number of sampling points.

the transmission of the microresonator. The transmission signal is recorded simultaneously with the calibration data during a laser scan on a separate channel of the oscilloscope. The resonances of the microresonator, similar to the FLC resonances, are detected by peak search algorithm and, owing to the calibrated laser scan, assigned a relative frequency. Due to non-linear resonance shifts it is important to only send a minimum required power to the microresonator.

Reconstruction of microresonator based combs

In a reconstruction experiment another fraction of the scanning diode laser light is combined with the generated Kerr-comb spectrum. As for the frequency calibration, a heterodyne beatnote is generated and filtered to generate a Kerr-comb line marker. Here, instead of two filters, a single filter is sufficient. A convenient choice is a 1.9 MHz low pass filter creating an electronic signal whenever the laser is within 1.9 MHz of a microresonator comb line.

The Kerr-comb marker signal is recorded simultaneously with the calibration data during a laser scan on a separate channel of the oscilloscope. An example of a typical data set is shown in Figure 2.15a.

D.2 Measurement of microcavity resonance width

The linewidth of a high-Q optical resonator can be measured by imposing modulation sidebands onto a laser that is scanning over the resonance. Three copies of the Lorentzian-shaped resonance are observed. The separation of the resonances in the scan corresponds to the modulation frequency, which yields a robust self-calibration, that allows to determine the resonance with. To avoid nonlinear resonance shifts it is important to perform the measurement at low power. Moreover, the scan parameters need to be chosen such that a constant scan velocity (in terms of optical frequency) is guaranteed over a sufficiently wide frequency window. Figure D.6 illustrates this method.
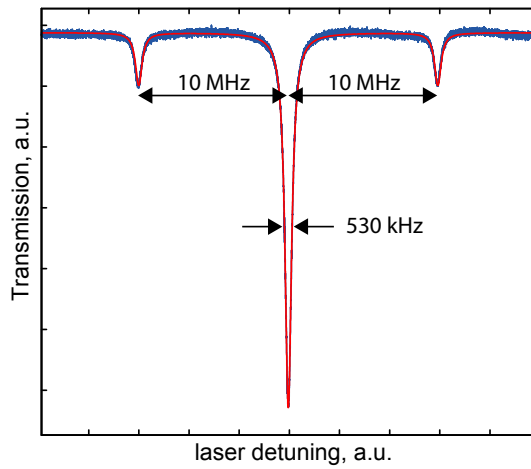

Figure D.6: Measurement of a microcavity resonance width. A phase modulated laser is scanned over a cavity resonance yielding the blue trace. The two smaller replica of the resonance are separated from the the main resonance by a distance corresponding to the modulation frequency (here: 10 MHz). The modulation sidebands provide the frequency calibration to determine the full-width at half maximum of the resonance (here: 530 kHz). The red line shows a triple-Lorentzian fit used for data analysis.